Available online at www.sciencedirect.com

ScienceDirect

Advances in Space Research 58 (2016) 2255–2268

ADVANCES IN SPACE RESEARCH (a COSPAR publication)

www.elsevier.com/locate/asr

Numerical simulation of the post-Newtonian equations of motion for the near Earth satellite with an application to the LARES satellite

Kyoung-Min Roh [a,*], Sergei M. Kopeikin [b,c], Jung-Ho Cho [a]

[a] Korea Astronomy and Space Science Institute, Daejeon 34055, Republic of Korea
[b] Department of Physics and Astronomy, 322 Physics Bldg., University of Missouri, Columbia, MO 65211, USA
[c] Siberian State University of Geosystems and Technologies, Plakhotny Street 10, Novosibirsk 630108, Russia

Received 20 May 2016; received in revised form 8 July 2016; accepted 9 August 2016
Available online 18 August 2016

Abstract

We study the post-Newtonian perturbations in the orbit of a near-Earth satellite by integrating them with a high-fidelity orbit propagation software KASIOP. The perturbations of the orbital elements are evaluated for various cases from a low-Earth orbit to a geostationary one, and from an equatorial to a polar orbit. In particular, the numerical simulation is applied to the LARES-like satellite under a realistic orbital configuration. The relativistic perturbations include the Schwarzschild term, the effects of Lense-Thirring precession, and the post-Newtonian term due to the quadrupole moment of the Earth as well as the post-Newtonian gravitoelectric and gravitomagnetic forces, which are produced by the tidal potential of the solar system bodies, are also modeled. The latter three terms are usually ignored in most orbit-propagation software. The secular variations of the orbital elements are evaluated from the orbital positions propagated for a half year. For a medium altitude orbit like that of the LARES mission, the magnitude of the relativistic perturbations ranges from the order of 10^{-7} m/s^2 by the Schwarzschild effect to 10^{-15} m/s^2 by the relativistic tidal effects. The orbital integration shows that the secular variations in three orbital elements – the ascending node, the argument of perigee, and the mean anomaly at epoch – are larger than the systematic error as results of the relativistic perturbations. The magnitudes of the secular variation are investigated in terms of the orbital altitude, inclination, and the size of each perturbation force. The numerical simulation rendered in this study shows that the secular post-Newtonian perturbations with the magnitude lying beyond the Schwarzschild and the Lense-Thirring effects need to be taken into account in current and upcoming space geodesy missions.

Keywords: Post-Newtonian; Orbit propagation; General relativity; Space Geodesy; Earth Quadrupole Moment

1. Introduction

Nowadays, the Earth-orbiting satellites play a critical role for space geodesy. The precise orbit determination is a main tool to determine a number of important fundamental properties in astronomy and geodesy. Namely the whole process of estimating the orbital position is the key to understand the Earth system like the gravitational field, reference frame, and even climate change. As there are increasing demands for the more accurate products like the gravitational field or the reference frame than ever before, the more precise orbital dynamic models should be developed. The Post-Newtonian (PN) relativistic perturbations cannot be ignored any longer in satellite's equations of motion. The International Earth Rotation Service and Reference Systems Service (IERS) have provided the relativistic references models and guidelines for processing the Earth-related measurements and they started to include the PN perturbation to IERS Standards (1992) (McCarthy, 1992). However, at that time, only the Schwarzschild solution of general relativity – the largest

* Corresponding author.
E-mail address: kmroh@kasi.re.kr (K.-M. Roh).

http://dx.doi.org/10.1016/j.asr.2016.08.009
0273-1177/

PN correction based on the spherical-symmetric gravitational field approximation – was suggested to be incorporated to the equations of motion. In 2000, the International Astronomical Union (IAU) released a series of resolutions for reference time scales and spatial coordinates with two origins, namely, the solar system barycentric and geocentric, and the equations of motion in the framework of general relativity (Soffel et al., 2003). These resolutions are based on the two formulations developed independently by Kopejkin (1988), Brumberg and Kopejkin (1989a, 1989b), and Damour et al. (1991, 1992, 1993, 1994) that defined the reference systems in the framework of the first PN approximation of general relativity. To accept these resolutions, the IERS Convention (2003) included the additional PN perturbing forces to the equations of motion of the Earth satellites, more specifically, Lense-Thirring force and de Sitter Precession (McCarthy and Petit, 2004). However, there are also other terms like the PN term due to the quadrupole moment of the Earth and the PN tidal gravitational field caused by the external bodies. These terms have not been included yet because their magnitude was considered to be too small to be measured compared to the Schwarzschild and Lense-Thirring terms.

The motivation of this study is to investigate the effects of the full first PN corrections through a numerical simulation under a realistic situation. Recent technological advances in measurements from space geodesy mission stimulate to reconsider the full PN theory of motion of satellites formulated by Brumberg and Kopejkin (1989a) and Damour et al. (1991, 1992, 1993, 1994). For example, the LAGEOS satellites and LARES measure the frame-dragging effect with an accuracy about 5% and have a goal to measure it up to about 1% of accuracy or even better (Ciufolini et al., 2009, 2015, 2016). Brumberg (2004) also suggested that the relativistic quadrupole perturbation needs to be taken into account, though the PN tidal effect due to the third-body might be ignored.

The PN relativistic perturbations in this study are considered as correction terms to the Newtonian equations of motion, therefore the equations of motion are integrated based on the integration technique that has been worked out in the Newtonian perturbation theory. There are another approaches to model an orbit around the Earth within the framework of general relativity (Pireaux et al., 2006; Kostić et al., 2015). These methods directly integrate four-dimensional equations of motion which are formulated using the metric tensor defined in space around the Earth. However, these full-relativistic approaches have difficulties to implement non-conservative perturbations originating in the Newtonian framework because all non-conservative force models, i.e., radiation pressures, atmospheric drag, etc., are still modeled with the Newtonian reference coordinates and time.

In the present study, the full PN equations of motion by Brumberg and Kopejkin (1989a) are numerically investigated with the help of a highly sophisticated orbit propagation model – KASIOP (Roh and Choi, 2014). The PN corrections due to the Earth potential are modeled considering only J2 term, while the Newtonian gravitational potential is calculated taking into account all spherical harmonics up to 70-by-70 degree. All planets in the solar system, the Sun, and the Moon are taken into account in calculating the PN tidal potential. The properties of the PN perturbations and their effects on the orbital elements are investigated for near circular orbits ranging from a low Earth orbit to the geostationary altitude and also from the equatorial to the polar orbit. The general results of the numerical simulation are applied to the LARES satellite which is the latest mission dedicated to the precise measurement of the Lense-Thirring effect. The present article is composed as follows. In Section 2, the brief summary of the PN formulas applied in this study and the issues related to the actual implementation in the numerical algorithm are addressed. The essential features of the orbit propagation software used in this study is also explained in Section 2. The results of the numerical analysis and the application to the LARES orbital case are presented in Section 3. Concluding remarks and resume of the study are presented in Section 4.

2. Implementation of the relativistic equations of motion

This section gives a brief introduction to the theory of the PN equations of motion of the Earth satellites and also addresses some issues which are to be resolved for practical implementation of the numerical technique used for integration of the relativistic perturbations. The problem is that the PN equations of motion and numerical models entering these equations are based on different relativistic coordinate systems and time scales. One needs to figure out what is the most optimal way to deal with the differences between the coordinates and time scales in terms of accuracy, efficiency and readability of the numerical integration algorithm. We also provide the mathematical method for calculation of the PN relativistic term due to the quadrupole moment of the Earth and describe the main features of the software used in the present study along with its numerical errors.

2.1. The first post-Newtonian perturbations in the geocentric coordinate

The PN equations of motion for near-Earth bodies with respect to the geocentric coordinate derived by Brumberg and Kopejkin (1989a) are used in the study. Spacetime is curved in general relativity and the motion of bodies inside the solar system is mathematically described using a metric tensor. The total gravitational field of the solar system defines the metric tensor and it is well known in the global barycentric coordinates $(t, \boldsymbol{r})$, where t is the barycentric coordinate time and $\boldsymbol{r}$ is the barycentric spatial vector. Therefore, the equations of motion in the barycentric system can be easily formulated. However, in order to describe

the motion with respect to the Earth in the local coordinates $(\hat{t}\hat{\boldsymbol{r}})$, the local metric should be defined in the near-Earth space. The local geocentric metric should be matched to the barycentric metric by means of the appropriate relativistic transformation. Here, $\hat{t}$ is the geocentric coordinate time and $\hat{\boldsymbol{r}}$ is the geocentric spatial components at $\hat{t}$. Brumberg and Kopejkin (1989a) defined the relativistic coordinate systems through matching the global and local metrics approximated up to the first PN terms at the overlapping region of the two metrics. The local metric determined by the matching method can be used to formulate the equations of motion of a test particle (satellite) in the geocentric coordinates as a geodesic line of the particle. The details of the mathematical derivation of the relativistic equations of motion of the near-Earth bodies can be found in the paper by Brumberg and Kopejkin (1989a) and are not provided over here.

Brumberg and Kopejkin (1989a) showed that the PN equations of motion of the Earth satellites, which are to be numerically integrated, can be expressed as the sum of three parts,

$$\frac{d^2\hat{\boldsymbol{r}}}{d\hat{t}^2} = \boldsymbol{a}_N + \boldsymbol{a}_{NC} + \frac{1}{c^2}\sum_{i=1}^{6}\boldsymbol{\Phi}_i, \tag{1}$$

where $\boldsymbol{a}_N$ is the Newtonian acceleration vector, and $\boldsymbol{a}_{NC}$ is non-conservative acceleration vector including the atmospheric drag and the radiation pressures from the Sun and the Earth. The specific forces and models for $\boldsymbol{a}_N$ and $\boldsymbol{a}_{NC}$ will be described in Section 2.3. The $\boldsymbol{\Phi}_i$ are the first PN perturbations which are divided into six terms (Brumberg and Kopejkin, 1989a). The investigation of each PN perturbation's effects is a main goal of this study. For the purpose of clarifying the article, the exact expression for each $\boldsymbol{\Phi}_i$ with explanatory remarks are presented in Appendix A. The physical meaning of each PN correction is as follows; $\boldsymbol{\Phi}_1$ is the relativistic Schwarzschild perturbation due to spherically symmetric component of geopotential, and $\boldsymbol{\Phi}_2$ is the Lense-Thirring force due to the Earth rotation which is also known as the frame-drag effect due to the Earth's gravitomagnetic field. These two corrections are the terms included into the current IERS Conventions (Petit and Luzum, 2010). There is also one more relativistic force in the IERS Conventions (2010), called as 'de Sitter Precession' which is related to the slow post-Newtonian precession of the spatial axes of the geocentric frame with respect to the barycentric one. Though these PN perturbations are relatively well known and widely applied to most of software dealing with geodetic measurements from space missions, we have included to the present paper the effects of $\boldsymbol{\Phi}_1$ and $\boldsymbol{\Phi}_2$ on the orbital elements for verification purpose. The perturbation $\boldsymbol{\Phi}_3$ is due to the Earth quadrupole moment, and $\boldsymbol{\Phi}_4$ is a nonlinear coupling of the monopole attracting force of the Earth and the gravitoelectric tidal field of the solar system bodies. Lastly, $\boldsymbol{\Phi}_5$ and $\boldsymbol{\Phi}_6$ are gravitomagnetic and gravitoelectric parts of the tidal perturbations due to the external bodies respectively (Brumberg and Kopejkin, 1989b; Klioner and Voinov, 1993). In case of $\boldsymbol{\Phi}_3$, there are several studies about the relativistic effect of Earth's quadrupole moment on the motion of satellites (Huang and Liu, 1992; Barker et al., 1981; Soffel et al., 1988), however they have been done separately from the current relativistic definitions of the geocentric and the barycentric reference systems. Will (2014) also indicated these earlier works had a deficiency in calculating the analytical variations of orbital elements.

2.2. Practical implementation issues

The implementation of the PN perturbations to an actual software has some issues to be resolved. In this section, the issues such as dealing with the mixed reference coordinates and time scales, and the calculation of the Earth quadrupole moment are explained. The detailed description about the orbit propagation software used in here are also presented in the next section.

2.2.1. Reference coordinate/time

The current IAU resolutions about reference coordinates and time scale for the geocentric bodies are the Geocentric Celestial Reference System (GCRS) and the Geocentric Coordinate Time (TCG), respectively. For the barycentric bodies of the solar system, the Barycentric Celestial Reference System (BCRS) and the Barycentric Coordinate Time (TCB) are recommended by the IAU's resolutions (Soffel et al., 2003). The directions of the reference systems are specified in IAU2006 Resolution B2, however these relativistic references are not widely applied yet even though the resolutions were released in 2000 (Kopeikin et al., 2011). The geocentric International Celestial Reference Frame (ICRF), which is defined as close as possible to the dynamical equinox at J2000.0 (hereafter J2000), and the Terrestrial Time (TT) are still dominant choices for most orbit propagation software of the near-Earth bodies. There are various reasons for this unpopularity. Firstly, the relativistic coordinates and time scale, i.e., the GCRS and TCG, are defined as close as possible to the J2000 and TT. The angular difference between two axes of the GCRS and the J2000, which is called 'frame-bias', is only about a level of 10 mas and time-independent. Therefore, the J2000 and TT are often used in the relativistic equations of motion instead of the GCRS/TCG, even though the equations are expressed in the relativistic references. However, this assumption can cause difficulties in analysis of the PN perturbations. For example, the differences in the solar system ephemerides caused by this assumption induce errors into the calculation of the relativistic tidal potential. Secondly, most numerical models embedded in the equations of motion, i.e., atmospheric density, solar activity, radiation of the Earth, etc., are still based on the J2000 and TT or other classical time scales like UTC. Therefore, if the GCRS and TCG are used as a reference frame of the numerical integration, additional calculations are required for the transformation between

the reference coordinates and time scales whenever calling the embedded numerical models.

Considering these two aspects, the combination of the J2000/TT is chosen as reference coordinates and time scale for integrating the equations of motion of satellites. It is also considered that the orbit propagation software used in here is based on the J2000 and TT (Roh and Choi, 2014). According to the IAU resolutions, the transformation between the GCRS and the J2000 is conducted using the following equation (Petit and Luzum, 2010):

$$\boldsymbol{x}_{GCRS} = \boldsymbol{B} \cdot \boldsymbol{x}_{J2000}, \tag{2}$$

where the matrix $\boldsymbol{B}$ stands for the coordinate transform matrix corresponds to the frame bias and is calculated using the SOFA library[1] in this study. Considering the frame bias $\boldsymbol{B}$ is constant matrix, the transformation equation for a velocity can be expressed as follows:

$$\boldsymbol{v}_{GCRS,TCG} = \boldsymbol{B} \cdot \boldsymbol{v}_{J2000,TT}(1 - L_G), \tag{3}$$

where $\boldsymbol{v}_{GCRS,TCG}$ is the velocity vector in the GCRS coordinate and TCG time scale, and $\boldsymbol{v}_{J2000,TT}$ is in the J2000 and TT. The $(1 - L_G)$ is the rate of TT time scale with respect to TCG, where $L_G = 6.969290134 \times 10^{-10}$ (Luzum et al., 2011).

The above transformation is applied to the calculation of the PN perturbations because the variables in the equations are with respect to the relativistic reference systems, namely, the GCRS and TCG for a satellite to be integrated as shown in Appendix A. Specifically, the position and velocity of the satellite should be transformed to the GCRS and TCG before calculating $\boldsymbol{\Phi}_i$, and the calculated accelerations should be transformed back to the J2000 and TT. For the ephemerides of the external bodies, most major models provide their ephemerides compatible to the BCRS, therefore no transformation needs. However, depending on software, the input epoch may need to be converted to TCB or TDB. In this study, the INPOP ephemerides model is used because it supports TT referenced time as an input epoch (Fienga et al., 2014; Standish, 1998; Pitjeva, 2013). Resultantly, it is required to apply the coordinate transformation from the J2000 and TT to the GCRS and TCG before calculating the PN perturbations, and the calculated PN corrections should be transformed back to the J2000 and TT system.

2.2.2. Quadrupole moments of the Earth

The calculations of $\boldsymbol{\Phi}_2$ and $\boldsymbol{\Phi}_3$ are related with the internal potential of the Earth. In this study, only the mass and quadrupole moment of the Earth are taken into account after expanding the internal potential using multipole moment tensors. In the general relativistic expression, the definitions of the mass and quadrupole moment have the additional PN corrections to the Newtonian one (Damour et al., 1994; Barker et al., 1981). However, these relativistic corrections to the mass and quadrupole moment due to the Earth internal gravitational field are ignored in this study, because their contribution is negligibly small (Brumberg and Kopejkin, 1989b).

The quadrupole moment of the Earth, namely the moment of inertia is calculated with the assumption of the Earth as an oblate spheroid. The actual calculation of the moment of inertia of the Earth is based on the relation between the inertia tensor and the geopotential coefficients (Chao and Gross, 1987), and the dynamic flattening value from Mihaila and Vilcu (2012). Applying the assumption of the rotating Earth with a constant angular velocity around the polar axis, the $\boldsymbol{\Phi}_2$ can be expressed with a more specified form as shown in the IERS Conventions (2010).

2.3. Orbit propagation model

Investigating the first PN equations of motion through a numerical simulation is highly dependent on the properties of the orbit propagation software to which the equations are implemented. In here, the orbit propagation software is briefly introduced to clarify the scope and the limit of the current simulation. Since the first PN perturbations are very tiny forces, the PN equations of motion should be applied to a high-precision orbit propagation software, which is called a target software hereafter. In this study, the KASIOP developed by the Korea Astronomy and Space Science Institute is used as the target software (Choi, 2014; Roh and Choi, 2014). Besides the PN equations of motion themselves, the implementation results can be affected by lots of parameters like numerical models for space environments and even the way the program designed. Therefore, it needs to introduce the essential features of the orbit propagation software used for implementing the PN equations of motion.

The target software's reference system is based on the J2000 and TT as mentioned in the previous section. The conservative perturbing forces modeled in here include the ones due to non-symmetrical geopotential up to 70 by 70 degree and its tidal variations, and the gravitational attractions with the solar system bodies. For the non-conservative forces, the atmospheric drag and the radiation pressures from the Sun and the Earth are modeled. Lastly, the guidelines in the IERS Conventions (2010) are used in the calculations of the precession, nutation, librations angles, etc. Table 1 summarizes the lists of the specific models and the numerical methods in this study. There is no standard method to evaluate the target software since a high-precision orbit propagation software is coupled with many parameters as mentioned earlier in this section and it is often not straightforward to match all of these parameters (Vallado, 2005). However, Choi (2014) evaluated the KASIOP's quality through fitting its ephemerides with the other one generated by using the Bernese package and the two ephemerides are matched with a couple of cm levels for the GPS case without any parameter adjustments from the default values (Dach et al., 2009). Considering that this value is at the level of the most

[1] Available at http://www.iausofa.org/2015_0209_C/sofa/manual.pdf.

Table 1
Summary of the model used in this study.

Item	Applied Model
Geopotential	
Zero-tide geopotential	EGM 2008, 70 × 70 (Pavlis et al., 2012)
Solid Earth/Solid Earth Pole/Ocean Pole Tide	IERS Convections (2010)
Ocean Tide	FES 2004 (Lyard et al., 2006)
Earth Rotation	
Precession-Nutation	IAU 2006/2000
Earth Rotation Parameters	IERS EOP C04 (Bizouard and Gambis, 2009)
Numerical Method	
Integration	10th order Summed Adams-Bashforth-Moulton (Montenbruck and Gill, 2011), 60s of the step size
Interpolation	10th order Lagrangian
Space Environments	
Atmospheric density	JB2008 (Bowman et al., 2012)
Earth Radiation	Rodriguez-Solano et al. (2011)
Solar system ephemeris	INPOP 13c

achievable orbit estimation results for the GPS orbit, the KASIOP can be thought to be compatible to the Bernese's orbit model which is used at one of the analysis center of the International GNSS Service.

Along with the overall scope of the propagation software, one needs to check the magnitude of its numerical systematic error of the software to see whether the PN correction terms can be resolved. Even though no perturbation is applied to the orbital integration like two-body motion, there can be some sources to cause truncation errors i.e., numerical integration, interpolating tabular data of the polar motion and so on. To evaluate the size of the numerical error of the target software solely, the variations of the orbital elements are calculated through comparing two orbits, one from two months of orbit propagation without any perturbation and the other from the analytical two-body solutions of Kepler's equation. A LAGEOS-2-like orbit is selected for this test, namely, a semi-major axis of 12,163 km, an inclination of 52.64 degree, and an eccentricity of 0.0135 (Ciufolini et al., 2016). The only semi-major axis and the argument of perigee show deviations from their original values. As depicted Fig. 1, the deviation of the semi-major axis (Δa) shows a typical truncation error at the level of 0.01 mm and the maximum error of the argument of perigee ($\Delta\omega$) is the level of 2.5 μas. From these results, the systematic error of the orbit propagator can be identified and the orbital variations larger than these values are considered to be meaningful results in this study.

There are a couple of things to be noted. The J2000 and TT are used as reference systems in this simulation in order to minimize the number of transformation between references, and also to inherit the legacies of the existing models as much as possible. However, there may be various ways to implement the first PN equations of motion depending on applications and a target software. In case of the calculation of the Earth quadrupole moment, though the Earth is assumed as a spherical ellipsoidal in here, it can be also evaluated including more geopotential coefficients depending on a progress of measurement technology in the future.

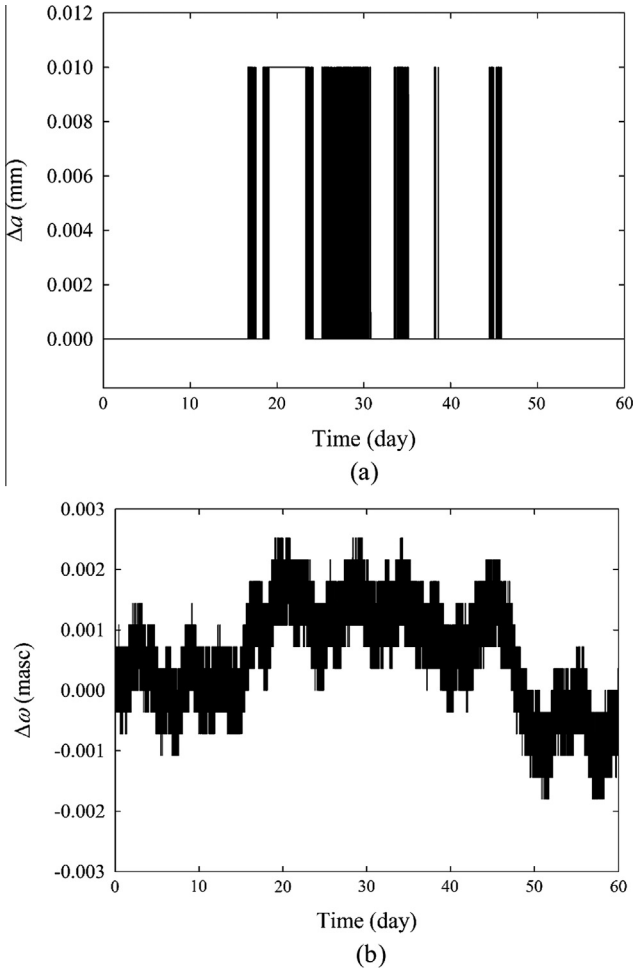

Fig. 1. Numerical truncation errors for the semi-major axis and the argument of perigee.

3. Numerical simulation

The simulation results for each PN perturbation are presented in this section. Firstly, the effects of the PN perturbations for the LAGEOS-2 orbit are tested to determine a proper simulation strategy. Then, the properties of each PN term are extensively investigated for various orbital cases. Among the results, the effect of the PN term due to the quadrupole moment of the Earth is especially interesting, since this term is the largest perturbation except the Schwarzschild and the Lense-Thirring terms whose properties have been studied widely (Ciufolini et al., 2009, 2015, 2016). Finally, the extensive numerical simulation of the PN perturbations is conducted to the LARES satellite which is expected to give the finest measurements ever to determine the Lense-Thirring effect.

Table 2
The variations of the orbital elements due to the PN terms.

		$\dot{a}$ (mm/yr)	$\dot{e}$	$\dot{i}$ (mas/yr)	$\dot{\Omega}$ (mas/yr)	$\dot{\omega}$ (mas/yr)	$\dot{M}$ (mas/yr)	Log $10(F_N)_{max}$ (m/s^2)
2-Body Based Case	$\boldsymbol{\Phi}_1$	-10^{-3}	10^{-13}	–	–	3349.67	−10369.83	−15.5
	$\boldsymbol{\Phi}_2$	0.01	–	10^{-5}	31.47	−57.29	0.75	−10.4
	$\boldsymbol{\Phi}_3$	0.02	–	10^{-3}	−0.91	0.12	0.81	−11.9
	$\boldsymbol{\Phi}_4$	-10^{-3}	–	–	10^{-3}	−0.02	0.53	−14.9
	$\boldsymbol{\Phi}_5$	−0.03	–	–	-10^{-4}	0.04	2.47	−14.0
	$\boldsymbol{\Phi}_6$	0.02	–	0.01	0.02	−0.04	0.27	13.6
Full-Per. Based Case	$\boldsymbol{\Phi}_1$	−0.06	-10^{-9}	0.01	2.96	3301.41	−10321.81	
	$\boldsymbol{\Phi}_2$	0.02	10^{-11}	−0.02	31.50	−56.45	−1.26	
	$\boldsymbol{\Phi}_3$	-10^{-5}	-10^{-11}	-10^{-3}	−0.91	0.70	3.09	
	$\boldsymbol{\Phi}_4$	−0.02	10^{-14}	10^{-4}	10^{-3}	0.04	1.13	
	$\boldsymbol{\Phi}_5$	−0.01	10^{-11}	10^{-4}	10^{-3}	−0.08	0.86	
	$\boldsymbol{\Phi}_6$	10^{-3}	–	10^{-3}	0.02	−0.01	−0.80	

3.1. Strategy for simulating the PN perturbations

The properties of each PN perturbation can be tested through comparing two orbits, i.e., with and without a specific PN term, if the PN forces have no coupling with other perturbations. Therefore, it is needed to check how much coupling exists between the PN terms and the other perturbations included in this study. In addition to the magnitude of the coupling, the most measurable orbital elements can be revealed from this test. The amount of the coupling is evaluated by comparing two types of simulations – the one without any classical perturbations like two-body motion and the other including all perturbations described in the previous section, i.e., $(2-\text{body}+\boldsymbol{\Phi}_i)-(2-\text{body})$ and $(\boldsymbol{a}_N+\boldsymbol{a}_{NC}+\boldsymbol{\Phi}_i)-(\boldsymbol{a}_N+\boldsymbol{a}_{NC})$. For this test, a half-year orbit propagation is performed for an LAGEOS-2 orbit. The spacecraft is also modeled like LAGEOS-2 satellite which has a cannonball shape with a large mass of 405.38 kg and a small radius of 300 mm in order to reduce the non-conservative perturbations. The simulation date is arbitrarily chosen to Oct. 30, 2008.

Table 2 summarizes the secular variations (Δ_S) for the orbital elements (a, e, i, Ω, ω, M_0) calculated through a linear regression method. The conversion from the Cartesian coordinate to the orbital elements is made using the method in Montenbruck and Gill (2011). The secular variations of a, e, and i in Table 2 are within or near numerical error. The other elements, which show the secular variations larger than the level of the systematic error, are investigated more deeply. Firstly, the secular variation of the ascending node can be interpreted through the relation with the normal directional forces (F_N) of the PN perturbations shown in the last column of Table 2, where the direction of F_N is defined to orthogonal to position and velocity vector. The time histories of the absolute values of F_N for the PN perturbations are depicted in Fig. 2. The maximum values of F_N in the last column of Table 2 as well as Fig. 2 show that the relative size of $\Delta_S\Omega$ in Table 2 is the direct result of the relative magnitude of F_N as expected from the differential equation of Ω in Euler-Gauss form,

$$\frac{d\Omega}{dt}=\frac{r\sin(f+\omega)}{na^2\sqrt{1-e^2}\sin i}F_N, \tag{4}$$

where r, f, and n mean radial distance from the center of mass, the true anomaly, the mean motion, respectively (Kopeikin et al., 2011). This fact also means that at least F_N is uncoupled with the other perturbations and the derivation of Ω is the most probable measurement to detect the PN perturbation. The largest magnitude of $\Delta_S\Omega$ comes from $\boldsymbol{\Phi}_2$ i.e., the Lense-Thirring effect. The second largest $\Delta_S\Omega$ is caused by the quadrupole moment of the Earth, i.e., $\boldsymbol{\Phi}_3$ whose property is investigated more in later test.

The argument of perigee also shows the distinctive variations rather than the other elements. However, the coupling effects on $\Delta_S\omega$ are a bit larger than those of $\Delta_S\Omega$. This coupling is caused by the fact that $\dot{\omega}$ is a function of the radial (F_R) and tangential (F_T) components as well as the normal one as shown in the differential equation for ω,

$$\frac{d\omega}{dt}=-\cos i\frac{d\Omega}{dt}+\frac{\sqrt{1-e^2}}{nae}\left[-F_R\cos f+F_T\left(1+\frac{r}{p}\right)\sin f\right]. \tag{5}$$

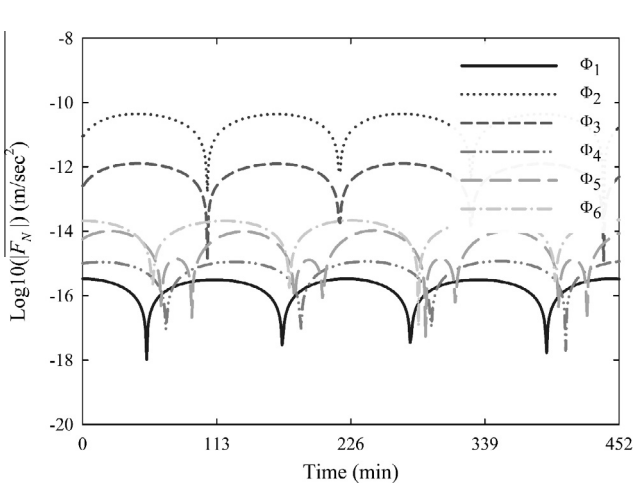

Fig. 2. The normal component accelerations of the PN perturbations for LAGEOS-2 orbit.

Additionally, the argument of perigee is less stable than the node value under the non-conservative perturbations (Ciufolini et al., 2009). Because of these reasons, the Lense-Thirring effect from the LAGEOS-1,2 satellites is achieved through calculating the secular variation of Ω rather than ω. Lastly, there are also some secular variations of the mean anomaly at epoch ($\Delta_S M_0$). The value $\Delta_S M_0$ is the largest at $\boldsymbol{\Phi}_1$ case as expected. However, the second largest one is caused by $\boldsymbol{\Phi}_3$ even though $\boldsymbol{\Phi}_2$ is the second largest perturbation. The reason is that the size $\Delta_S M_0$ is the results of coupling of $\Delta_S\Omega$ and $\Delta_S\omega$ as well as the radial components of perturbation as shown in the differential equation of M_0 in Euler-Gauss form;

$$\frac{dM_0}{dt} = -\sqrt{1-e^2}\left(\frac{d\omega}{dt} + \cos i \frac{d\Omega}{dt}\right) - \frac{2r}{na^2}F_R. \tag{6}$$

Like $\Delta_S\omega$, it is very difficult to measure or estimate the value $\Delta_S M_0$ because of complicated coupling with the other elements. Fig. 3 depicts the two largest cases besides the Schwarzschild and the Lense-Thirring terms, namely, the variations of Ω due to $\boldsymbol{\Phi}_3$ and ω due to $\boldsymbol{\Phi}_5$. The variation of $\Delta_{S,\boldsymbol{\Phi}3}\omega$ of Fig. 3(b) also shows the short and long periodic pattern because $\boldsymbol{\Phi}_5$ is related with the relativistic tidal potential generated by the solar system bodies. Even though its periodic properties, it is worth to investigate its secular variation to compare with the other PN perturbations. This periodic property is not the main focus of this study but this can be investigated in future work. From the analysis of the results in this subsection, the numerical simulations for various orbital cases of the next subsection are based on the 2-body based strategy because this method can focus on the PN perturbations themselves without considering any coupling effects with the other perturbations.

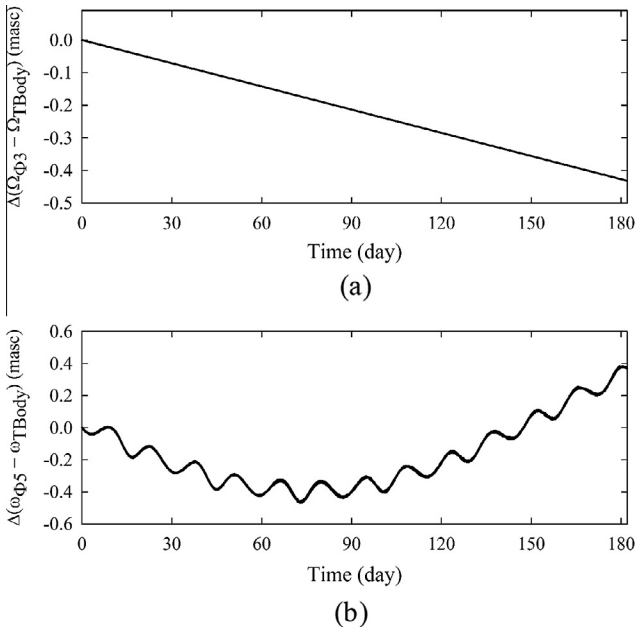

Fig. 3. Variation of orbital elements. (a) $\Delta\Omega$ due to $\boldsymbol{\Phi}_3$ and (b) $\Delta\omega$ due to $\boldsymbol{\Phi}_5$.

The investigation of the PN perturbation's effect on the orbital elements is also concentrated on $\Delta_S\Omega$ than other elements.

3.2. Tests for various orbital cases

Based on the result of the previous simulation, the method of the two-body plus one specific PN term is applied to various orbital cases. The investigations in this subsection are focused on the two most detectable elements – Ω and ω. A more realistic simulation is also tested for the LARES satellite later in this section. Three semi-major axes of 7000 km, 12,800 km, and 42,164 km which are the typical value of low-Earth-orbit (LEO), medium Earth orbit (MEO) which is the same altitude with the LAGEOS's, and geostationary orbit (GEO). For each altitude, the secular variations of the orbital elements are calculated for the inclinations of 2°, 20°, 40°, 60°, 80° and 90°. In all simulations, the eccentricity is set to 0.002 because a near-circular orbit is the most probable one for a space geodesy mission. The other elements, namely, true anomaly, argument of perigee, and ascending node are set to 0°. By the way, the lowest inclination is set to 2° instead of 0° for easier evaluation of the secular variation of the ascending node. Total 18 orbits are propagated for 6 months and then the secular variations of the orbital elements for each case are calculated.

As indicated in the previous test, the ascending node and the argument of perigee are the most noticeable elements to investigate the PN perturbations. Fig. 4 summarizes the resulting $\Delta_S\Omega$ and $\Delta_S\omega$ in terms of the orbital inclination and altitude for the cases when its maximum magnitude is larger than the level μas/yr. Namely, Fig. 4(a)–(c) are $\Delta_S\Omega$ for the cases of $\boldsymbol{\Phi}_{2,3,6}$, and Fig. 4(d)–(i) depicted $\Delta_S\omega$ for all $\boldsymbol{\Phi}_i$. However, it is harder to extract which directional force causes $\Delta_S\omega$ than in case of $\Delta_S\Omega$, because $\Delta_S\omega$ is coupled with the orbital inclination and is also a function of all three – radial, along, and cross track components of perturbing force.

In the case of the Schwarzschild perturbation, the radial acceleration is dominant relative to the other components and its value mainly depends on the orbital radius because it comes from the spherical symmetric component of the Earth. Therefore, the values $\Delta_S\omega$ caused by $\boldsymbol{\Phi}_1$ in Fig. 4 (d) are the same in all inclinations of each altitude, and they increase as the orbital altitude becomes lower. The Lense-Thirring perturbations on Ω and ω plotted in Fig. 4 (a) and (e) show that $\Delta_S\Omega$ has no dependency on the orbital inclination whereas the argument of perigee does. This phenomenon can be understood from Fig. 5 showing the pattern of the decomposed accelerations for $\boldsymbol{\Phi}_2$ along the orbital phase ($=\omega + f$) of the LEO case. In Fig. 5, the orbital phase at 0° and 180° correspond to the ascending and the descending node, respectively. The magnitude of the cross-track component at every orbital phase in Fig. 5 increases sinusoidally as the inclination varies from 0° to 90°. This sinusoidal variation is canceled by 'sin i' term in

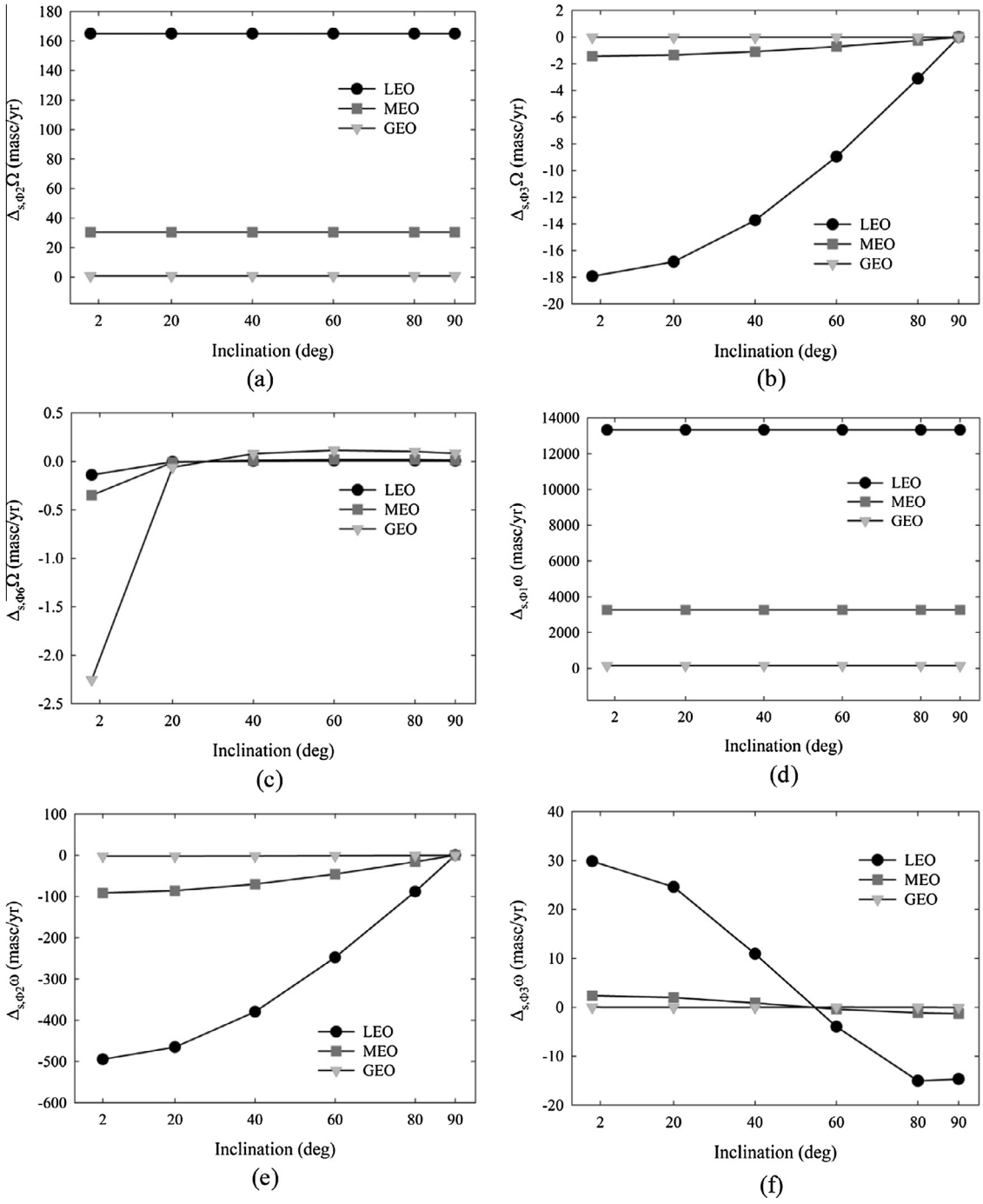

Fig. 4. The secular variations of Ω and ω due the PN perturbations in various orbital cases.

Eq. (4), therefore $\Delta_S\Omega$ due to $\boldsymbol{\Phi}_2$ becomes independent of the orbital inclination. Unlike the ascending node, $\Delta_S\omega$ due to $\boldsymbol{\Phi}_2$ becomes lower as the inclination goes higher, because the magnitude of the cross-track component is larger than the other ones by 1–2 orders and also $\Delta_S\omega$ is affected by a factor of 'cos i' to $\Delta_S\Omega$ as seen in the first term of Eq. (5).

In this simulation, the PN relativistic term due to the multipole moments of the Earth, $\boldsymbol{\Phi}_3$, take into account only the Earth's quadrupole moment. Fig. 4(b) and (f) show that $\Delta_S\Omega$ and $\Delta_S\omega$ due to $\boldsymbol{\Phi}_3$, respectively. Unlike the case of $\boldsymbol{\Phi}_2$, the value $\Delta_S\Omega$ in Fig. 4(b) decreases as the inclination goes from an equatorial to a polar orbit. This dependency can be explained through the equation of $\dot{\Omega}$ which is affected by only the normal component of perturbation as shown in Eq. (4). Namely, if multiply a unit vector, $\boldsymbol{k}$ to $\boldsymbol{\Phi}_3$ (see Appendix A) where $\boldsymbol{k}$ is the normal to the orbital plane, the only remaining term is $\hat{I}_E\hat{\boldsymbol{r}}$ because the vector $\boldsymbol{k}$ is normal to both position and velocity vectors. Assuming that the quadrupole moment has diagonal terms

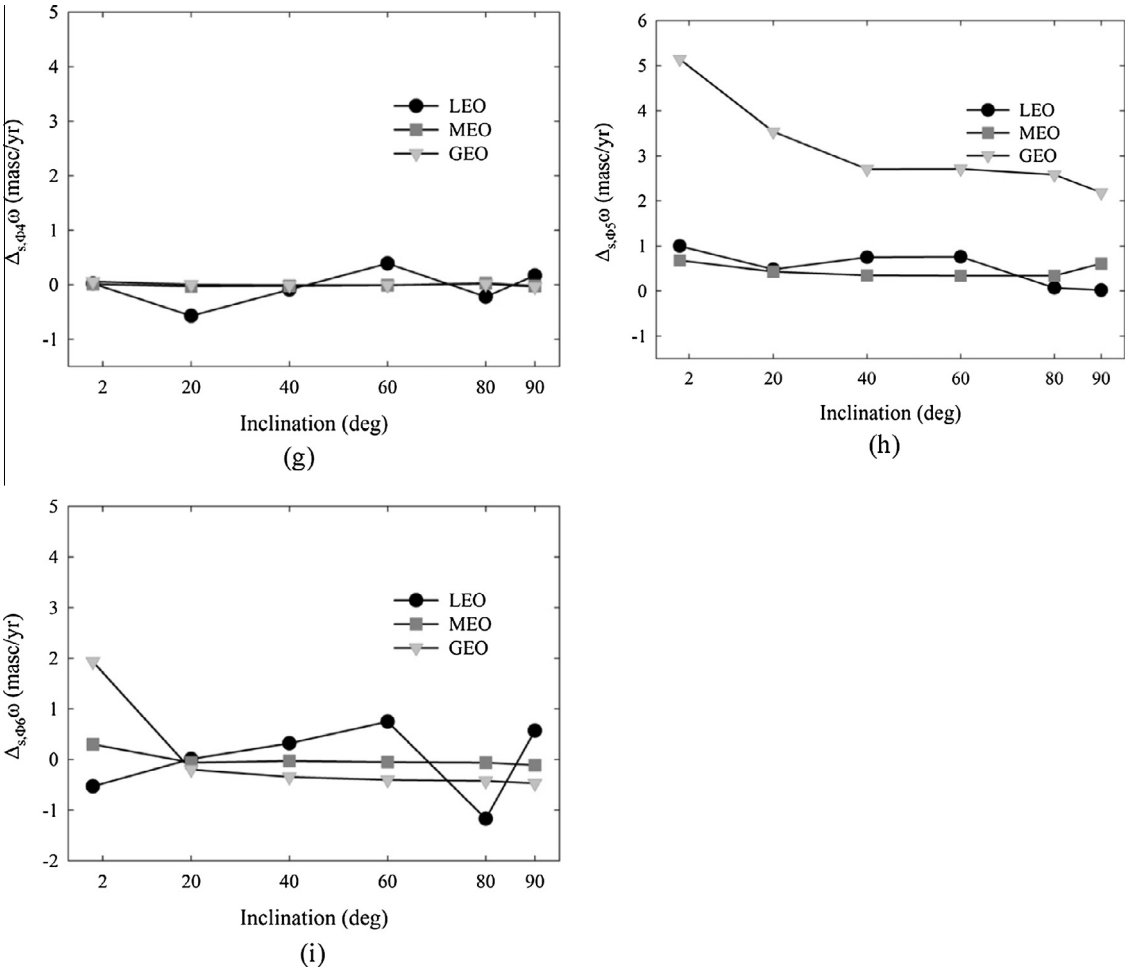

Fig 4. *(continued)*

of $\hat{I}^E_{11} = \hat{I}^E_{22} \neq \hat{I}^E_{33}$ and zero off-diagonal terms, the normal component of $\boldsymbol{\Phi}_3$ can be rewritten as follows,

$$\boldsymbol{\Phi}_3 \cdot \boldsymbol{k} = 3\frac{G}{\hat{r}^5}\left(\hat{v}^2 - 4\frac{G\widehat{M}_E}{\hat{r}}\right)\hat{z}k_z, \tag{7}$$

where k_z is the z-component of the vector $\boldsymbol{k}$. Substituting $\hat{z}$ and k_z to '$\hat{r}\sin i$' and 'cos i', respectively, the normal component of $\boldsymbol{\Phi}_3$ becomes a function of 'sin $2i$', namely, the cross-track force becomes the largest at an inclination of 45°. This property can be also seen in Fig. 6 which plots the decomposed forces of $\boldsymbol{\Phi}_3$ for various inclinations of the LEO case. Resultantly, according to Eq. (4), the amount of $\Delta_S\Omega$ due to $\boldsymbol{\Phi}_3$ becomes a function of cos i as shown in Fig. 4(b). The magnitude of $\Delta_S\Omega$ due to $\boldsymbol{\Phi}_3$ reaches up to 10% in LEO equatorial orbit and about 5% in an equatorial MEO as can be seen Fig. 4(a) and (b). In addition to the above tests, the values of $\Delta_{S,\boldsymbol{\Phi}2}\Omega$ and $\Delta_{S,\boldsymbol{\Phi}3}\Omega$ for the LAGEOS-1 satellite are calculated using the parameter given in the article of Ciufolini et al. (2016). The effects of $\boldsymbol{\Phi}_2$ and $\boldsymbol{\Phi}_3$ on the ascending node of the LAGEOS-1 are $\Delta_{S,\boldsymbol{\Phi}2}\Omega = 30.64$ mas/yr, $\Delta_{S,\boldsymbol{\Phi}3}\Omega = 0.49$ mas/yr, respectively. The ratio, $\Delta_{S,\boldsymbol{\Phi}3}\Omega/\Delta_{S,\boldsymbol{\Phi}2}\Omega$, of the LAGEOS-1 is about 1.6% which is slightly less than that of the LAGEOS-2 shown in Table 2, namely, 2.8% ($\Delta_{S,\boldsymbol{\Phi}2}\Omega = 31.47$ mas/yr, $\Delta_{S,\boldsymbol{\Phi}3}\Omega = -0.91$ mas/yr). This result indicates that the relativistic perturbation of the Earth quadrupole moment can be analyzed in case of an equatorial orbit, since Ciufolini et al. (2016) shows that the Lense-Thirring effects can be measured with an accuracy about 5% and also expected up to 1% (Ciufolini et al., 2009).

The decomposed accelerations for $\boldsymbol{\Phi}_4$, $\boldsymbol{\Phi}_5$ and $\boldsymbol{\Phi}_6$ in case of the MEO depicted in Figs. 7–9 show that the maximum acceleration ranges from a level of 10^{-14} m/s^2 for $\boldsymbol{\Phi}_6$, and $\boldsymbol{\Phi}_5$ to a level of 10^{-15} m/s^2 for $\boldsymbol{\Phi}_4$. Since the other three PN terms are related to the relativistic tidal potential generated by the solar system bodies, their decomposed accelerations and their effects on the orbital elements in Figs. 7–9 are both quite different from the previous PN terms related to the Earth's own gravitational potential in some aspects. Firstly, the effects of these relativistic tidal perturbations become larger as the altitude goes higher, namely, the largest at the equational GEO case. Secondly, the radial and along track accelerations of $\boldsymbol{\Phi}_4$ to $\boldsymbol{\Phi}_6$ have little dependency on the inclination, though they have a little higher fluctuation in medium inclinations. Lastly, the normal component of accelerations is the weakest at

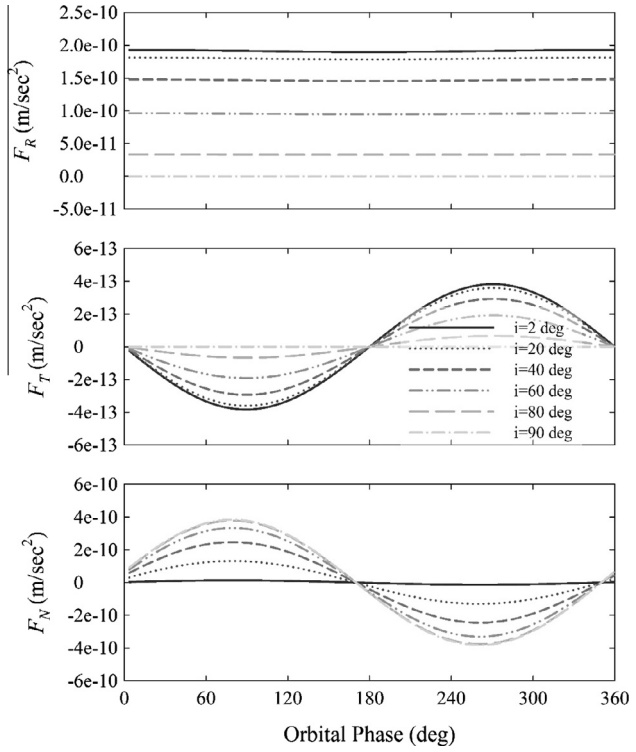

Fig. 5. The radial, along and cross track acceleration of $\boldsymbol{\Phi}_2$ for the LEO case.

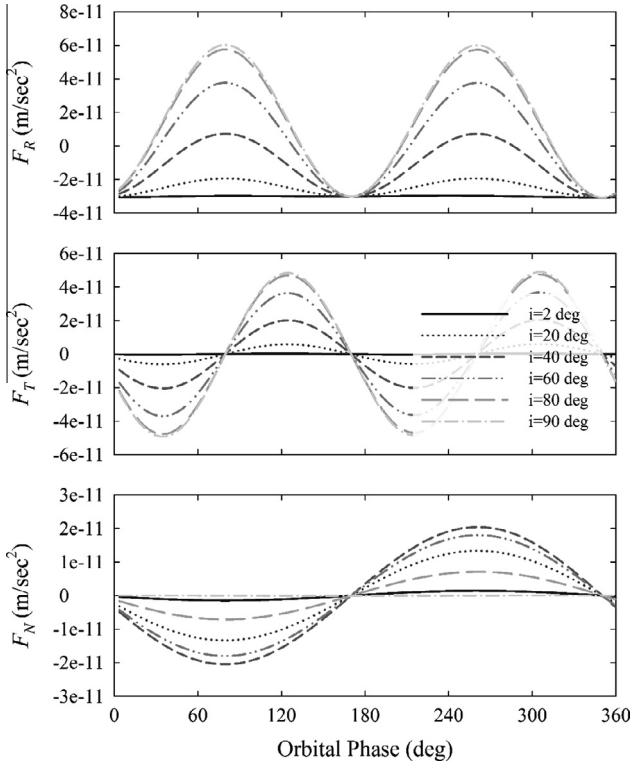

Fig. 6. The radial, along and cross track acceleration of $\boldsymbol{\Phi}_3$ for the LEO case.

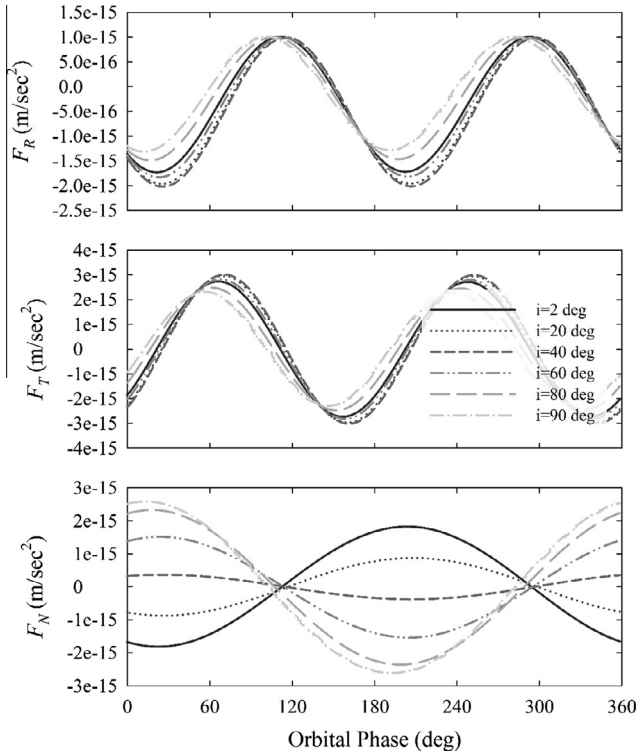

Fig. 7. The radial, along and cross track acceleration of $\boldsymbol{\Phi}_4$ for the MEO case.

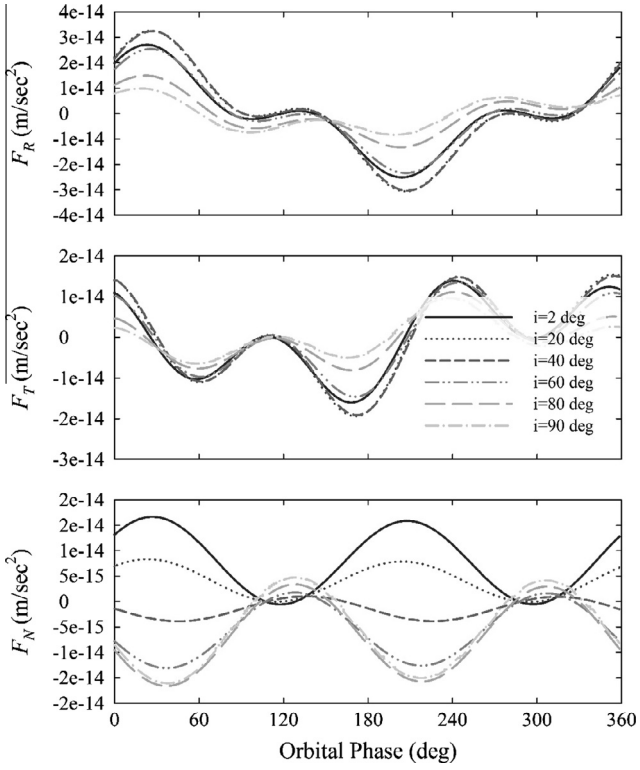

Fig. 8. The radial, along and cross track acceleration of $\boldsymbol{\Phi}_5$ for the MEO case.

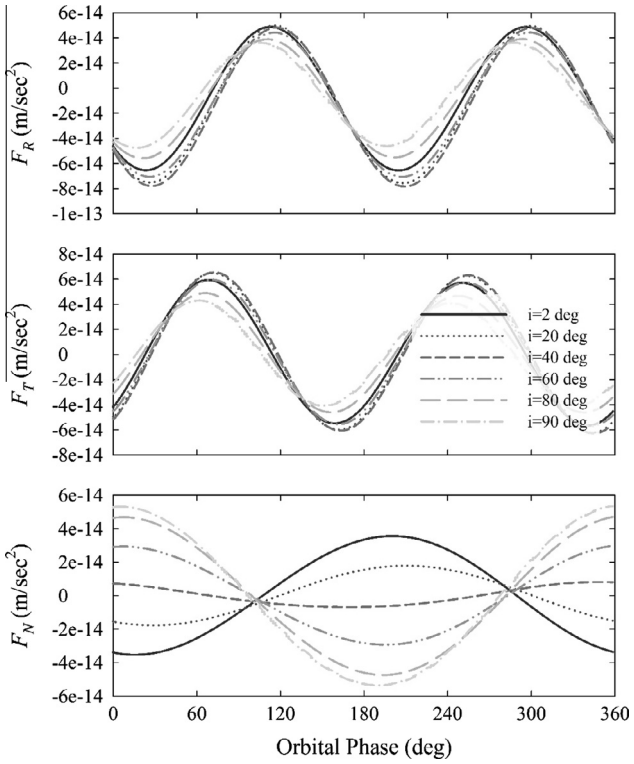

Fig. 9. The radial, along and cross track acceleration of $\boldsymbol{\Phi}_6$ for the MEO case.

medium inclination and the forces of the lower and higher inclination have the opposite direction with similar magnitude.

3.3. Test for LARES case

The last test is conducted with realistic configurations for the LARES satellite, Laser RElativity Satellite of the Italian Space Agency, which was launched 2012 with semi-major axis of 7820 km, $e \approx 0.008$ and $i \approx 69.5°$ (Ciufolini et al., 2015). The measurements from the LARES is expected to determine the Lense-Thirring effect up to 1% with combined help by the recent Earth gravitational model achieved by the GRACE mission (Tapley et al., 2004). The simulation in this section is conducted through comparing two orbits, the one including the full perturbations as well as the PN terms and the other with the same option except one specific PN term. In here, the two PN perturbations, $\boldsymbol{\Phi}_2$ and $\boldsymbol{\Phi}_3$ are tested because they are the most probable terms to be detected. Actually, the precise determination of $\Delta_S\Omega$ due to $\boldsymbol{\Phi}_2$ is one of the LARES's main mission. The value of $\Delta_S\Omega$ due to $\boldsymbol{\Phi}_3$ is also calculated because it is found that the effect of $\boldsymbol{\Phi}_3$ would be larger than the target error level of the LARES mission from the previous test. This configuration can be considered the most probable situation in actual measurement processing.

The magnitudes of the perturbations included in this test are compared in Fig. 10. The total sum of the first PN perturbations are compared with the other classical one in Fig. 10(a) and the individual first PN perturbations are plotted in Fig. 10(b). Because of the low area-to-mass ratio of the LARES, the first PN perturbation is larger than any non-conservative ones.

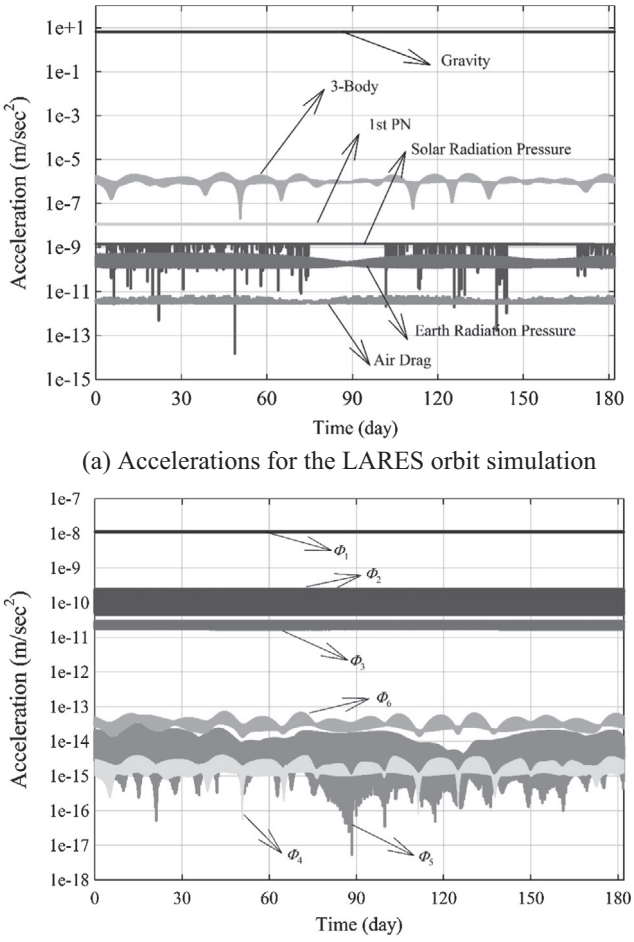

(a) Accelerations for the LARES orbit simulation

(b) The first Post-Newtonian Accelerations for the LARES orbit simulation

Fig. 10. The comparison of accelerations on the LARES satellites.

The orbits are propagated for 6 months, and the values $\Delta_S\Omega$ due to $\boldsymbol{\Phi}_2$ and $\boldsymbol{\Phi}_3$ are calculated about 118.5 mas/yr and −3.91 mas/yr, respectively. These values agree well to the previous result and the size of $\Delta_S\Omega$ due to $\boldsymbol{\Phi}_3$ is about 4% of the Lense-Thirring effect. This result indicates that the term $\boldsymbol{\Phi}_3$ needs to be included the LARES mission data processing.

4. Conclusion

The first post-Newtonian perturbations for the near-Earth satellite are numerically simulated and investigated through implementing the post-Newtonian equations of motion to a highly sophisticated orbit propagation software. The software is based on the geocentric ICRF and TT as reference coordinates and time scale, and the relativistic references are used when required in a way to

minimize redundancy in coordinates and time conversion. The numerical simulation shows that the PN relativistic perturbations can be divided to two types. One is from $\boldsymbol{\Phi}_1$ to $\boldsymbol{\Phi}_3$ which are also known as the Schwarzschild term, the Lense-Thirring term, and the PN relativistic term due to the quadrupole moment of the Earth, respectively. These three PN perturbations are related to the Earth gravitational potential. The other one from $\boldsymbol{\Phi}_4$ to $\boldsymbol{\Phi}_6$ is caused by the relativistic tidal potentials by the external bodies in the solar system. The former is stronger in the LEO than the GEO, while the latter shows the opposite pattern. The magnitudes of the PN perturbations in the case of the LARES orbit are an order of 10^{-8} m/s^2 for the Schwarzschild term, 10^{-9} m/s^2 for the Lense-Thirring term, 10^{-11} m/s^2 for the PN term due to the quadrupole moment of the Earth, and 10^{-14}–10^{-15} m/s^2 for the tidal potential related ones. Especially, the effect of $\boldsymbol{\Phi}_3$, which is not yet widely applied, is larger than that from the atmospheric drag, even though the LARES has a small cannonball shape with a high density to reduce non-conservative perturbations. The secular variation of the ascending node due to the relativistic effect of the quadrupole moment of the Earth can reach up to 10% of that due to the Lense-Thirring effect in an equatorial LEO case.

The magnitude of some post-Newtonian perturbations is still very tiny to be measured in the near-Earth environments. However, since the measurement technology and the Earth gravitational models keep improving, there is a higher requirement for more complete dynamic models for the Earth observing satellite mission. From this numerical simulation of this study, the properties of the post-Newtonian perturbations are investigated and some of them are needed to be included in space geodesy missions.

Acknowledgement

We thank the anonymous referees for valuable comments and suggestions for improving the presentation of the manuscript. This study has been supported by the 2016 Primary Project of the Korea Astronomy and Space Science Institute (KASI) (Project: Operation of Space Geodetic Infra-facilities and Research on Astronomical Almanac). The work of Sergei Kopeikin has been supported by the Grant No. 14-27-00068 of the Russian Science Foundation (RSF).

Appendix A

Vector form expression of $\boldsymbol{\Phi}_i$ $(i = 1, \ldots, 6)$

$$\boldsymbol{\Phi}_1 = \frac{G\widehat{M}_E}{|\hat{\boldsymbol{r}}|^3}\left[\left(\frac{4G\widehat{M}_E}{|\hat{\boldsymbol{r}}|} - \hat{v}^2\right)\hat{\boldsymbol{r}} + 4(\hat{\boldsymbol{r}}\cdot\widehat{\boldsymbol{v}})\widehat{\boldsymbol{v}}\right] \tag{A.1}$$

$$\boldsymbol{\Phi}_2 = \frac{2G}{|\hat{\boldsymbol{r}}|^3}C\widehat{\omega}\left[\widehat{\boldsymbol{v}}\times\boldsymbol{s} + \frac{3\hat{z}}{|\hat{\boldsymbol{r}}|^2}(\hat{\boldsymbol{r}}\times\widehat{\boldsymbol{v}})\right] \tag{A.2}$$

$$\begin{aligned}\boldsymbol{\Phi}_3 = {} & \frac{4G^2\widehat{M}_E}{|\hat{\boldsymbol{r}}|^6}\left\{-2\mathrm{diag}(\boldsymbol{I}_E)\hat{\boldsymbol{r}} - 3\boldsymbol{I}_E\hat{\boldsymbol{r}} + \frac{9}{|\hat{\boldsymbol{r}}|^2}[(\boldsymbol{I}_E\hat{\boldsymbol{r}})^T\cdot\hat{\boldsymbol{r}}]\hat{\boldsymbol{r}}\right\} \\ & + \frac{3}{2}\frac{G}{|\hat{\boldsymbol{r}}|^5}\hat{v}^2\left\{\mathrm{diag}(\boldsymbol{I}_E) + 2\boldsymbol{I}_E\hat{\boldsymbol{r}} - \frac{5}{|\hat{\boldsymbol{r}}|^2}[(\boldsymbol{I}_E\hat{\boldsymbol{r}})^T\cdot\hat{\boldsymbol{r}}]\hat{\boldsymbol{r}}\right\} \\ & + 6\frac{G}{|\hat{\boldsymbol{r}}|^5}\hat{\boldsymbol{v}}\left\{-\mathrm{diag}(\boldsymbol{I}_E)(\hat{\boldsymbol{r}}\cdot\hat{\boldsymbol{v}}) - 2[(\boldsymbol{I}_E\hat{\boldsymbol{v}})^T\cdot\hat{\boldsymbol{r}}]\right. \\ & \left. + \frac{5}{|\hat{\boldsymbol{r}}|^2}[(\boldsymbol{I}_E\hat{\boldsymbol{r}})^T\cdot\hat{\boldsymbol{r}}](\hat{\boldsymbol{r}}\cdot\hat{\boldsymbol{v}})\right\}\end{aligned} \tag{A.3}$$

$$\boldsymbol{\Phi}_4 = -4\frac{G\widehat{M}_E}{|\hat{\boldsymbol{r}}|}\overline{\boldsymbol{U}}_D\cdot\hat{\boldsymbol{r}} + 2\frac{GM_E}{|\hat{\boldsymbol{r}}|^3}[(\overline{\boldsymbol{U}}_D\hat{\boldsymbol{r}})^T\cdot\hat{\boldsymbol{r}}]\hat{\boldsymbol{r}} \tag{A.4}$$

$$\begin{aligned}\boldsymbol{\Phi}_5 = {} & -4[(\overline{\boldsymbol{U}}_D\hat{\boldsymbol{v}})^T\cdot\hat{\boldsymbol{r}}]\hat{\boldsymbol{v}} + |\hat{\boldsymbol{v}}|^2\overline{\boldsymbol{U}}_D\hat{\boldsymbol{r}} + 4\begin{bmatrix}(\overline{\boldsymbol{V}}_D^1\hat{\boldsymbol{v}})^T\cdot\hat{\boldsymbol{r}}\\(\overline{\boldsymbol{V}}_D^2\hat{\boldsymbol{v}})^T\cdot\hat{\boldsymbol{r}}\\(\overline{\boldsymbol{V}}_D^3\hat{\boldsymbol{v}})^T\cdot\hat{\boldsymbol{r}}\end{bmatrix} \\ & + 4\begin{bmatrix}(\overline{\boldsymbol{V}}_{1D}\hat{\boldsymbol{r}})^T\cdot\hat{\boldsymbol{v}}\\(\overline{\boldsymbol{V}}_{2D}\hat{\boldsymbol{r}})^T\cdot\hat{\boldsymbol{v}}\\(\overline{\boldsymbol{V}}_{3D}\hat{\boldsymbol{r}})^T\cdot\hat{\boldsymbol{v}}\end{bmatrix} - 4[(\overline{\boldsymbol{U}}_D\hat{\boldsymbol{v}})^T\cdot\hat{\boldsymbol{r}}]\boldsymbol{v}_E + 4(\boldsymbol{v}_E\cdot\hat{\boldsymbol{v}})(\overline{\boldsymbol{U}}_D\hat{\boldsymbol{r}}) \\ & + 2(\dot{\boldsymbol{a}}_E\cdot\hat{\boldsymbol{v}})\hat{\boldsymbol{r}} - 2(\hat{\boldsymbol{r}}\cdot\hat{\boldsymbol{v}})\dot{\boldsymbol{a}}_E\end{aligned} \tag{A.5}$$

$$\begin{aligned}\boldsymbol{\Phi}_6 = {} & \boldsymbol{F}[(\overline{U}_D)^T\boldsymbol{r}_E] + \overline{\boldsymbol{U}}_D(\boldsymbol{F}^T\hat{\boldsymbol{r}}) - 4\begin{bmatrix}(\overline{\boldsymbol{V}}_{1D}\hat{\boldsymbol{r}})^T\cdot\boldsymbol{v}_E\\(\overline{\boldsymbol{V}}_{2D}\hat{\boldsymbol{r}})^T\cdot\boldsymbol{v}_E\\(\overline{\boldsymbol{V}}_{3D}\hat{\boldsymbol{r}})^T\cdot\boldsymbol{v}_E\end{bmatrix} \\ & + 2v_E^2(\overline{\boldsymbol{U}}_D\hat{\boldsymbol{r}}) - 2\overline{U}(\overline{\boldsymbol{U}}_D\hat{\boldsymbol{r}}) - \frac{1}{2}\boldsymbol{v}_E[(\overline{\boldsymbol{U}}_D\widehat{\boldsymbol{v}})\cdot\hat{\boldsymbol{r}}] \\ & - \frac{1}{2}(\overline{\boldsymbol{U}}_D\boldsymbol{v}_E)(\boldsymbol{v}_E\cdot\hat{\boldsymbol{r}}) + \overline{\boldsymbol{W}}_D\hat{\boldsymbol{r}} + \ddot{\overline{\boldsymbol{U}}}\hat{\boldsymbol{r}} + 2\left(\frac{\partial\dot{\overline{\boldsymbol{V}}}}{\partial\hat{\boldsymbol{r}}}\right)\hat{\boldsymbol{r}} \\ & + 2\left(\frac{\partial\dot{\overline{\boldsymbol{V}}}}{\partial\hat{\boldsymbol{r}}}\right)^T\hat{\boldsymbol{r}} - 3\boldsymbol{a}_E(\boldsymbol{a}_E\cdot\hat{\boldsymbol{r}}) - \boldsymbol{v}_E(\dot{\boldsymbol{a}}_E\cdot\hat{\boldsymbol{r}}) - (\hat{\boldsymbol{r}}\cdot\boldsymbol{v}_E)\dot{\boldsymbol{a}}_E\end{aligned} \tag{A.6}$$

Notations in the above equations are follows:

Subscript E indicates the Earth.

$\hat{\boldsymbol{r}} = [\hat{r}^1, \hat{r}^2, \hat{r}^3]^T$, $\hat{\boldsymbol{v}} = [\hat{v}^1, \hat{v}^2, \hat{v}^3]^T$, position and velocity vector in the GCRS system.

$\boldsymbol{r} = [r^1, r^2, r^3]^T$, $\boldsymbol{v} = [v^1, v^2, v^3]^T$, position and velocity vector in the BCRS system.

$\boldsymbol{I}_E$ = Moment of inertia of the Earth.

$\overline{\boldsymbol{U}}_D = \frac{\partial}{\partial\boldsymbol{r}}\left(\frac{\partial\overline{U}}{\partial\boldsymbol{r}}\right)^T$ where $\overline{U}$ is the gravitational potential due to the external bodies.

$\overline{\boldsymbol{V}}_D^j = \frac{\partial}{\partial\boldsymbol{r}}\left(\frac{\partial\overline{V}^j}{\partial\boldsymbol{r}}\right)^T$, $j = 1, 2, 3$. $\overline{\boldsymbol{V}} = [\overline{V}^1, \overline{V}^2, \overline{V}^3]$ is the gravitational vector potential due to the external bodies.

$\overline{\boldsymbol{V}}_{jD} = \frac{\partial}{\partial r^j}\left(\frac{\partial\overline{\boldsymbol{V}}}{\partial\boldsymbol{r}}\right)^T$, $j = 1, 2, 3$.

$\boldsymbol{a}_E$ = Acceleration of the Earth in the BCRS system (Brumberg and Kopejkin, 1989a).

$\boldsymbol{F}$ = Physically related to the angular velocity of rotation of the GCRS spatial axes, however this term ignored due to

its negligibly small effects (Brumberg and Kopejkin, 1989a).

$\overline{W}_D = \frac{\partial}{\partial r}\left(\frac{\partial \overline{W}}{\partial r}\right)^T$ where $\overline{W}$ is the auxiliary potential due to the external bodies.

References

Barker, B.M., O'Brien, G.M., O'Connell, R.F., 1981. Relativistic quadrupole moment. Phys. Rev. D (Particles and Fields) 24, 2332–2335. http://dx.doi.org/10.1103/PhysRevD.24.2332.

Bizouard, C., Gambis, D., 2009. The combined solution C04 for Earth orientation parameters consistent with international terrestrial reference frame 2005. In: Drewes, H. (Ed.), Geodetic Reference Frames: IAG Symposium Munich, Germany, 9–14 October 2006, Geodetic Reference Frames: IAG Symposium Munich, Germany, 9–14 October 2006. Springer, Berlin, Heidelberg, pp. 265–270. http://dx.doi.org/10.1007/978-3-642-00860-3_41.

Bowman, B., Tobiska, W.K., Marcos, F., Huang, C., Lin, C., Burke, W., 2012. A new empirical thermospheric density model JB2008 using new solar and geomagnetic indices. In: Presented at the AIAA/AAS Astrodynamics Specialist Conference and Exhibit. American Institute of Aeronautics and Astronautics, Reston, Virginia. http://dx.doi.org/10.2514/6.2008-6438.

Brumberg, V.A., 2004. On relativistic equations of motion of an Earth satellite. Celest. Mech. Dyn. Astron. 88, 209–225. http://dx.doi.org/10.1023/B:CELE.0000016821.33627.77.

Brumberg, V.A., Kopejkin, S.M., 1989a. Relativistic reference systems and motion of test bodies in the vicinity of the Earth. Nuovo Cimento B 103, 63–98. http://dx.doi.org/10.1007/BF02888894.

Brumberg, V.A., Kopejkin, S.M., 1989b. Relativistic theory of celestial reference frames. Reference Frames. http://dx.doi.org/10.1007/978-94-009-0933-5_6.

Chao, B.F., Gross, R.S., 1987. Changes in the Earth's rotation and low-degree gravitational field induced by earthquakes. Geophys. J. Int. 91, 569–596. http://dx.doi.org/10.1111/j.1365-246X.1987.tb01659.x.

Choi, B-K. (Ed.), 2014. High Precision GNSS Data processing Software Development: Status Report-2013180001. Korea Astronomy and Space Science.

Ciufolini, I., Paolozzi, A., Pavlis, E.C., Koenig, R., Ries, J., Gurzadyan, V., Matzner, R., Penrose, R., Sindoni, G., Paris, C., 2015. Preliminary orbital analysis of the LARES space experiment. Eur. Phys. J. Plus 130, 133–135. http://dx.doi.org/10.1140/epjp/i2015-15133-2.

Ciufolini, I., Paolozzi, A., Pavlis, E.C., Koenig, R., Ries, J., Gurzadyan, V., Matzner, R., Penrose, R., Sindoni, G., Paris, C., Khachatryan, H., Mirzoyan, S., 2016. A test of general relativity using the LARES and LAGEOS satellites and a GRACE Earth gravity model. Eur. Phys. J. C 76, 120–127. http://dx.doi.org/10.1140/epjc/s10052-016-3961-8.

Ciufolini, I., Paolozzi, A., Pavlis, E.C., Ries, J.C., Koenig, R., Matzner, R. A., Sindoni, G., Neumayer, H., 2009. Towards a one percent measurement of frame dragging by spin with satellite laser ranging to LAGEOS, LAGEOS 2 and LARES and GRACE gravity models. Space Sci. Rev. 148, 71–104. http://dx.doi.org/10.1007/s11214-009-9585-7.

Dach, R., Brockmann, E., Schaer, S., Beutler, G., Meindl, M., Prange, L., Bock, H., Jäggi, A., Ostini, L., 2009. GNSS processing at CODE: status report. J. Geod. 83, 353–365. http://dx.doi.org/10.1007/s00190-008-0281-2.

Damour, T., Soffel, M., Xu, C., 1991. General-relativistic celestial mechanics. I. Method and definition of reference systems. Phys. Rev. D 43, 3273–3307. http://dx.doi.org/10.1103/PhysRevD.43.3273.

Damour, T., Soffel, M., Xu, C., 1992. General-relativistic celestial mechanics II. Translational equations of motion. Phys. Rev. D 45, 1017–1044. http://dx.doi.org/10.1103/PhysRevD.45.1017.

Damour, T., Soffel, M., Xu, C., 1993. General-relativistic celestial mechanics. III. Rotational equations of motion. Phys. Rev. D 47, 3124–3135. http://dx.doi.org/10.1103/PhysRevD.47.3124.

Damour, T., Soffel, M., Xu, C., 1994. General-relativistic celestial mechanics. IV. Theory of satellite motion. Phys. Rev. D 49, 618–635. http://dx.doi.org/10.1103/PhysRevD.49.618.

Fienga, A., Manche, H., Laskar, J., Gastineau, M., Verma, A.K., 2014. INPOP New Release: INPOP13c. Available at <http://www.imcce.fr/fr/presentation/equipes/ASD/inpop/inpop13c.pdf>.

Huang, C., Liu, L., 1992. Analytical solutions to the four post-Newtonian effects in a near-earth satellite orbit. Celest. Mech. Dyn. Astron. 53, 293–307. http://dx.doi.org/10.1007/BF00052615, ISSN: 0923-2958.

Klioner, S.A., Voinov, A.V., 1993. Relativistic theory of astronomical reference systems in closed form. Phys. Rev. D 48, 1451–1461. http://dx.doi.org/10.1103/PhysRevD.48.1451.

Kopeikin, S., Efroimsky, M., Kaplan, G., 2011. Relativistic Celestial Mechanics of the Solar System. John Wiley & Sons, p. 731.

Kopejkin, S.M., 1988. Celestial coordinate reference systems in curved space-time. Celest. Mech. 44, 87–115. http://dx.doi.org/10.1007/BF01230709.

Kostić, U., Horvat, M., Gomboc, A., 2015. Relativistic positioning system in perturbed spacetime. Class. Quant. Grav. 32, 215004. http://dx.doi.org/10.1088/0264-9381/32/21/215004.

Luzum, B., Capitaine, N., Fienga, A., Folkner, W., Fukushima, T., Hilton, J., Hohenkerk, C., Krasinsky, G., Petit, G., Pitjeva, E., Soffel, M., Wallace, P., 2011. The IAU 2009 system of astronomical constants: the report of the IAU working group on numerical standards for fundamental astronomy. Celest. Mech. Dyn. Astron. 110, 293–304. http://dx.doi.org/10.1007/s10569-011-9352-4.

Lyard, F., Lefevre, F., Letellier, T., Francis, O., 2006. Modelling the global ocean tides: modern insights from FES2004. Ocean Dyn. 56, 394–415. http://dx.doi.org/10.1007/s10236-006-0086-x.

McCarthy, D.D., 1992. IERS Standards (1992). IERS Technical Note 13. Central Bureau of IERS.

McCarthy, D.D., Petit, G. (Eds.), 2004. IERS Conventions (2003). IERS Technical Note 32. Verlag des Bundesamts für Kartographie und Geodäsie, Frankfurt am Main.

Mihaila, I., Vilcu, A.-D., 2012. On the value of the dynamical flattening of the Earth. Romanian Astron. J. 22, 43–57.

Montenbruck, O., Gill, E., 2011. Satellite Orbits. Springer, Berlin.

Pavlis, N.K., Holmes, S.A., Kenyon, S.C., Factor, J.K., 2012. The development and evaluation of the Earth Gravitational Model 2008 (EGM2008). J. Geophys. Res. 117, B04406. http://dx.doi.org/10.1029/2011JB008916.

Petit, G., Luzum, B. (Eds.), 2010. IERS Conventions (2010). IERS Technical Note 36. Verlag des Bundesamts für Kartographie und Geodäsie, Frankfurt am Main.

Pireaux, S., Barriot, J.-P., Rosenblatt, P., 2006. (SC) RMI: A (S)emi-(C)lassical (R)elativistic (M)otion (I)ntegrator, to model the orbits of space probes around the Earth and other planets. Acta Astronaut. 59, 517–523. http://dx.doi.org/10.1016/j.actaastro.2006.04.006.

Pitjeva, E.V., 2013. Updated IAA RAS planetary ephemerides-EPM2011 and their use in scientific research. Sol. Syst. Res. 47, 386–402. http://dx.doi.org/10.1134/S0038094613040059.

Rodriguez-Solano, C.J., Hugentobler, U., Steigenberger, P., Lutz, S., 2011. Impact of Earth radiation pressure on GPS position estimates. J. Geod. 86, 309–317. http://dx.doi.org/10.1007/s00190-011-0517-4.

Roh, K.-M., Choi, B.-K., 2014. The effects of the IERS conventions (2010) on high precision orbit propagation. J. Astron. Space Sci. 31, 41–50. http://dx.doi.org/10.5140/JASS.2014.31.1.41.

Soffel, M., Klioner, S.A., Petit, G., Wolf, P., Kopeikin, S.M., Bretagnon, P., Brumberg, V.A., Capitaine, N., Damour, T., Fukushima, T., Guinot, B., Huang, T.Y., Lindegren, L., Ma, C., Nordtvedt, K., Ries, J.C., Seidelmann, P.K., Vokrouhlicky, D., Will, C.M., Xu, C., 2003. The IAU 2000 resolutions for astrometry, celestial mechanics, and metrology in the relativistic framework: explanatory supplement. Astron. J. 126, 2687–2706. http://dx.doi.org/10.1086/378162.

Soffel, M., Wirrer, R., Schastok, J., Ruder, H., Schneider, M., 1988. Relativistic effects in the motion of artificial satellites - the oblateness of the central body I. Celest. Mech. 42, 81–89. http://dx.doi.org/10.1007/BF01232949.

Standish, E.M., 1998. JPL Planetary and Lunar Ephemerides, DE405/LE405. JPL Interoffice Memorandum. Available at <ftp://ssd.jpl.nasa.gov/pub/eph/planets/ioms/de405.iom.pdf>.

Tapley, B.D., Bettadpur, S., Ries, J.C., Thompson, P.F., Watkins, M.M., 2004. GRACE measurements of mass variability in the Earth system. Science 305, 503–506. http://dx.doi.org/10.1126/science.1099192.

Vallado, D.A., 2005. An analysis of state vector propagation using differing flight dynamics program. In: AAS/AIAA Space Flight Mechanics Conference. AAS, Colorado, USA.

Will, C.M., 2014. Incorporating post-Newtonian effects in N-body dynamics. Phys. Rev. D 89, 044043-15. http://dx.doi.org/10.1103/PhysRevD.89.044043.